



# SnSe<sub>2</sub> nanocrystals coupled with hierarchical porous carbon microspheres for long-life sodium ion battery anode

Hui Chen<sup>1,2,3</sup>, Zijie Mu<sup>1</sup>, Yiju Li<sup>1</sup>, Zhonghong Xia<sup>1</sup>, Yong Yang<sup>1</sup>, Fan Lv<sup>1</sup>, Jinhui Zhou<sup>1</sup>, Yuguang Chao<sup>1</sup>, Jinshu Wang<sup>2</sup>, Ning Wang<sup>2,3</sup> and Shaojun Guo<sup>1,4,5\*</sup>

**ABSTRACT** Tin selenides have been attracting great attention as anode materials for the state-of-the-art rechargeable sodium-ion batteries (SIBs) due to their high theoretical capacity and low cost. However, they deliver unsatisfactory performance in practice, owing to their intrinsically low conductivity, sluggish kinetics and volume expansion during the charge-discharge process. Herein, we demonstrate the synthesis of SnSe<sub>2</sub> nanocrystals coupled with hierarchical porous carbon (SnSe<sub>2</sub> NCs/C) microspheres for boosting SIBs in terms of capacity, rate ability and durability. The unique structure of SnSe<sub>2</sub> NCs/C possesses several advantages, including inhibiting the agglomeration of SnSe<sub>2</sub> nanoparticles, relieving the volume expansion, accelerating the diffusion kinetics of electrons/ions, enhancing the contact area between the electrode and electrolyte and improving the structural stability of the composite. As a result, the as-obtained SnSe<sub>2</sub> NCs/C microspheres show a high reversible capacity (565 mA h g<sup>-1</sup> after 100 cycles at 100 mA g<sup>-1</sup>), excellent rate capability, and long cycling life stability (363 mA h g<sup>-1</sup> at 1 A g<sup>-1</sup> after 1000 cycles), which represent the best performances among the reported SIBs based on SnSe<sub>2</sub>-based anode materials.

**Keywords:** tin selenides, nanocrystals, hierarchical, sodium-ion batteries

## INTRODUCTION

As a promising alternative to lithium-ion batteries (LIBs), sodium-ion batteries (SIBs) have recently attracted

growing interest particularly for large-scale energy storage applications owing to the abundance and uniform distribution of sodium resource in the earth crust [1–5]. However, their electrochemical performances are severely hindered by severe volume variation and slow kinetics during insertion/extraction processes of sodium ions (Na<sup>+</sup>) due to the intrinsic larger ionic radius and heavier molar mass of sodium ion than lithium ion [6–11]. Particularly, most of anode materials that are suitable for LIBs could not be applied directly in SIBs [12–15]. Therefore, the exploitation of excellent anode materials with high specific capacity, outstanding Na-storage reversibility and excellent rate capability is urgently desirable but remains a challenge.

Recently, Sn-based materials, such as SnO<sub>2</sub> [16–19], SnS [20,21], SnS<sub>2</sub> [22–24], and Sn<sub>4</sub>P<sub>3</sub> [25,26], have attracted tremendous attention as promising anode materials for both LIBs and SIBs. As earth-abundant, environmental friendly, and chemically stable materials, tin selenides (including SnSe and SnSe<sub>2</sub>) have also been regarded as attractive anode materials for SIBs, yet seldom studied till now [27,28]. SnSe<sub>2</sub> is highlighted due to its unique layered structure and high interlayer spacing (6.14 Å for SnSe<sub>2</sub> vs. the diameter of 1.02 Å for Na<sup>+</sup>), which provides a fast channel for the transfer of ions and electrons [29,30]. Particularly, SnSe<sub>2</sub> as an anode material for SIBs demonstrates a high theoretical reversible capacity of 756 mA h g<sup>-1</sup> [31]. However, similar to other Sn-based materials, SnSe<sub>2</sub> is known for several drawbacks including

<sup>1</sup> Department of Materials Science & Engineering, College of Engineering, Peking University, Beijing 100871, China

<sup>2</sup> State Key Laboratory of Electronic Thin Film and Integrated Devices, University of Electronic Science and Technology of China, Chengdu 610054, China

<sup>3</sup> State Key Laboratory of Marine Resource Utilization in South China Sea, Hainan University, Haikou 570228, China

<sup>4</sup> BIC-ESAT, College of Engineering, Peking University, Beijing 100871, China

<sup>5</sup> Department of Energy and Resources Engineering, College of Engineering, Peking University, Beijing 100871, China

\* Corresponding author (email: [guosj@pku.edu.cn](mailto:guosj@pku.edu.cn))

the low electrical conductivity, huge volume variation and high mechanical stress/strain upon cycling, inevitably resulting in serious kinetic problems, making it difficult to fully take advantage of the conversion reactions, and thus leading to limited reversible capacity, cycle stability, and rate capability in practical application [29–32].

To solve these issues, herein, we report a facile strategy to prepare SnSe<sub>2</sub> nanocrystals coupled with hierarchical porous carbon (SnSe<sub>2</sub> NCs/C) microspheres. First, uniform stanniferous solid precursor microspheres were synthesized by a one-pot solvent-thermal method in the presence of stannous chloride and ascorbic acid in a mixed isopropanol/glycerol solution, which were subsequently transferred into SnO<sub>2</sub> NCs/C microspheres by the thermal treatment in Ar. Then, the as-prepared SnO<sub>2</sub> NCs/C microspheres underwent a simple selenization reaction to form SnSe<sub>2</sub> NCs/C microspheres, which were particularly attractive for solving the problems related to SIBs. The SnSe<sub>2</sub> NCs/C microspheres inhibits the agglomeration of SnSe<sub>2</sub> nanocrystals by separating them from each other, and greatly improves the conductivity as well as availability of electrode materials. The 3D hierarchical porous structure not only enhances the contact

area between the electrode and electrolyte, but also helps to suppress the volume expansion during charge-discharge processes. The SnSe<sub>2</sub> nanocrystals are small and uniformly anchor on the carbon networks, and thus accelerate the diffusion kinetics of electrons/ions and improve the stability of the structure. Benefiting from these structural advantages, the SIBs based on the as-prepared SnSe<sub>2</sub> NCs/C microspheres exhibit a high reversible specific capacity of 565 mA h g<sup>-1</sup> at 100 mA g<sup>-1</sup>, an excellent cycling stability (363 mA h g<sup>-1</sup> at 1 A g<sup>-1</sup> after 1000 cycles), and superior rate capability.

## RESULTS AND DISCUSSION

### Morphological and structural characterization

The design and synthetic process of the SnSe<sub>2</sub> NCs/C microspheres is schematically illustrated in Fig. 1a. Firstly, Sn-precursor (Sn-P) microspheres were facilely prepared by a one-pot solvent-thermal method in the presence of stannous chloride and ascorbic acid in a mixed isopropanol/glycerol solution. Subsequently, the uniform SnO<sub>2</sub> NCs/C microspheres were formed by annealing those Sn-precursor microspheres in Ar. Finally,

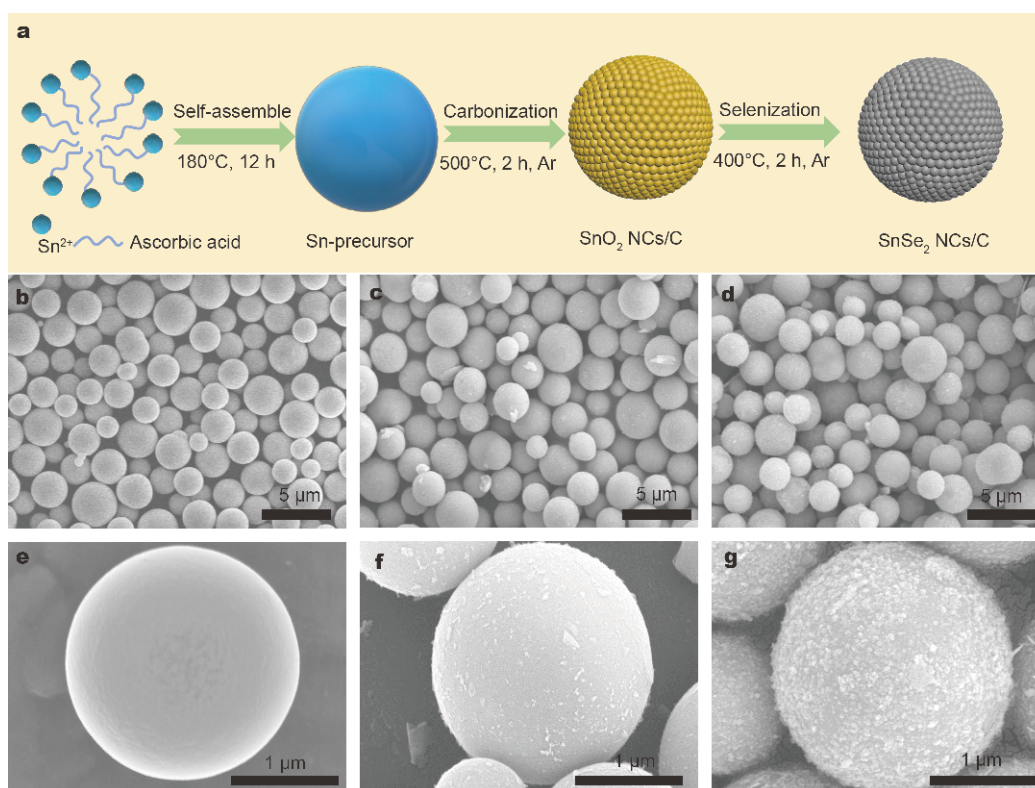


**Figure 1** (a) Schematic illustration of the formation process of SnSe<sub>2</sub> NCs/C microspheres. SEM images of the as-synthesized Sn-precursor microspheres (b, e); SnO<sub>2</sub> NCs/C microspheres (c, f) and SnSe<sub>2</sub> NCs/C microspheres (d, g).

the SnSe<sub>2</sub> NCs/C microspheres were obtained *via* simple selenization in Ar atmosphere.

The morphologies of the as-synthesized Sn-P microspheres, SnO<sub>2</sub> NCs/C microspheres, and SnSe<sub>2</sub> NCs/C microspheres were investigated with the scanning electron microscope (SEM) as shown in Fig. 1b–g. In Fig. 1b, e, the Sn-P particles have a size of ~2 μm with an ideal microsphere morphology. After the annealing treatment in Ar, the Sn-P microspheres are transformed to SnO<sub>2</sub> NCs/C microspheres, with the morphology and particle size unchanged (Fig. 1c, f). These SnO<sub>2</sub> NCs/C microspheres exhibit the hierarchical structure consisting of primary nanoparticles. After the selenization, the SnSe<sub>2</sub> NCs/C microspheres still retain the spherical morphology (Fig. 1d, g). Fig. 2a shows a typical SnSe<sub>2</sub> NCs/C microsphere with the corresponding energy dispersive X-ray spectrum (EDS) elemental mapping shown in Fig. 2b. The atomic ratio of Sn/Se is about 1:2, confirming the chemical composition of SnSe<sub>2</sub> NCs/C. All of the expected elements of the composite can be recognized. Transmission electron microscopy (TEM) and high-re-

solution TEM (HRTEM) were carried out to further investigate the microstructure of the SnSe<sub>2</sub> NCs/C. As shown in Fig. 2c, the SnSe<sub>2</sub> NCs/C microspheres have a diameter of approximately 2 μm, in accordance with the SEM results. A highly porous hollow interior structure densely dispersed with small nanoparticles (SnSe<sub>2</sub>) can be confirmed by the non-uniform contrast. The HRTEM image in Fig. 2d shows that the SnSe<sub>2</sub> NCs with the size of nanometers (~10 nm) are embedded in the carbon matrix. The clear lattice fringes indicate their good crystallinity. The resolved lattice fringes of these SnSe<sub>2</sub> NCs with an interplanar spacing of 0.29 nm correspond to (101) crystal facets of SnSe<sub>2</sub>. The compact and robust SnSe<sub>2</sub> NCs/C microspheres assembled by spherical nanoparticles are able to increase the contact area between the electrode and electrolyte, relieve the volume expansion during the insertion/extraction of Na<sup>+</sup>, and accelerate the diffusion kinetics of Na-ion due to the shortened Na diffusion distances.

The crystal structures of the as-synthesized Sn-P microspheres, SnO<sub>2</sub> NCs/C microspheres, and SnSe<sub>2</sub> NCs/C

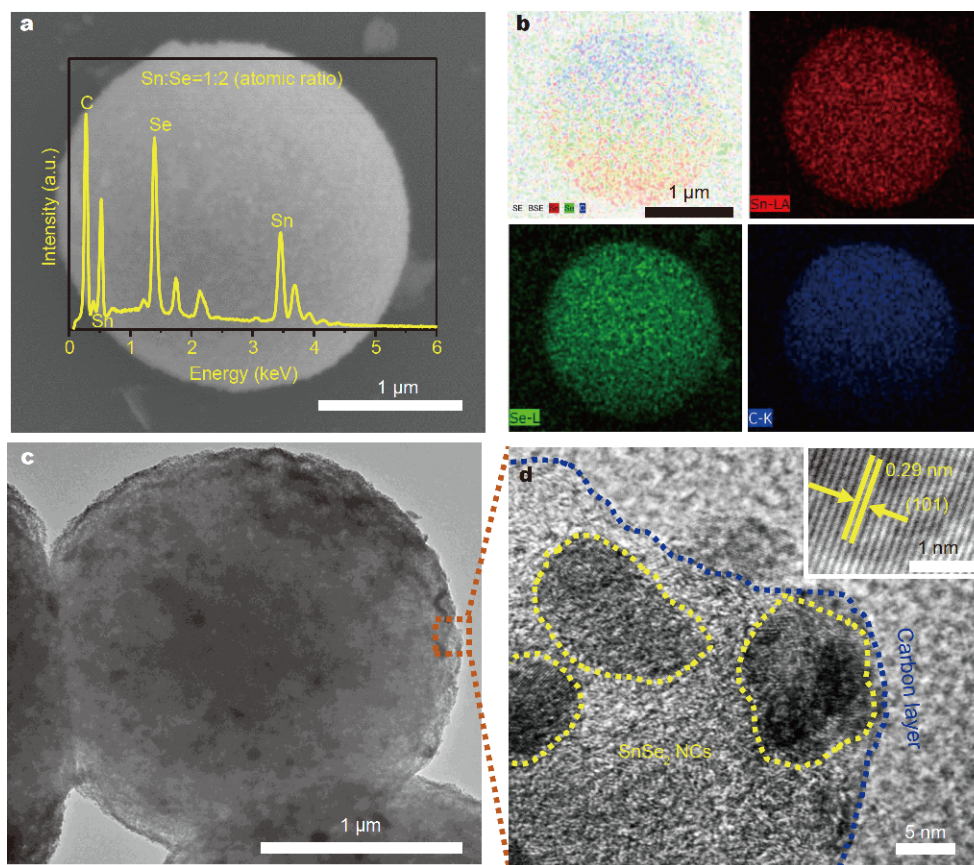


**Figure 2** (a) Typical SEM image of SnSe<sub>2</sub> NCs/C microspheres and the corresponding elemental mapping of (b) tin, selenium, and carbon elements. (c) TEM and (d) HRTEM images of SnSe<sub>2</sub> NCs/C.

microspheres were characterized by the powder X-ray diffraction (PXRD) (Fig. 3a), showing the Sn-P microspheres with low crystallinity. After annealing in Ar at 500°C for 2 h, the as-prepared Sn-P microspheres can be converted to SnO<sub>2</sub> (JCPDS No. 41-1445). In addition, for the PXRD of final products, all Bragg peaks can be indexed to the hexagonal phase SnSe<sub>2</sub> (JCPDS No. 23-0602), suggesting that the SnO<sub>2</sub> is completely converted into the phase-pure SnSe<sub>2</sub> *via* the thermal selenization. Furthermore, no significant carbon diffraction peaks are observed, suggesting its amorphous state. Fig. S1 presents the hexagonal layered crystal structure of SnSe<sub>2</sub>. The specific surface area (SSA) of the SnSe<sub>2</sub> NCs/C microspheres was further characterized with the Brunauer-

Emmett-Teller (BET) analysis (Fig. 3b). The SnSe<sub>2</sub> NCs/C possesses a large SSA of 73.9 m<sup>2</sup> g<sup>-1</sup> and a high pore volume of 0.068 cm<sup>3</sup> g<sup>-1</sup>, in good agreement with TEM and HRTEM results. The SnSe<sub>2</sub> NCs/C with large SSA is beneficial to increasing the contact area between the electrode and electrolyte, improving electrolyte transfer and carrier transport kinetics, and thus boosting the performance of SIBs. The amorphous carbon content in the SnSe<sub>2</sub> NCs/C is about 15 wt%, as measured by inductively coupled plasma mass spectrometry (ICP). As control experiment, the bulk SnSe<sub>2</sub> was synthesized by annealing Sn with Se powder in Ar at 500°C for 2 h, and characterized with the PXRD (Fig. S2) and SEM (Fig. S3).

In order to further investigate the chemical composi-

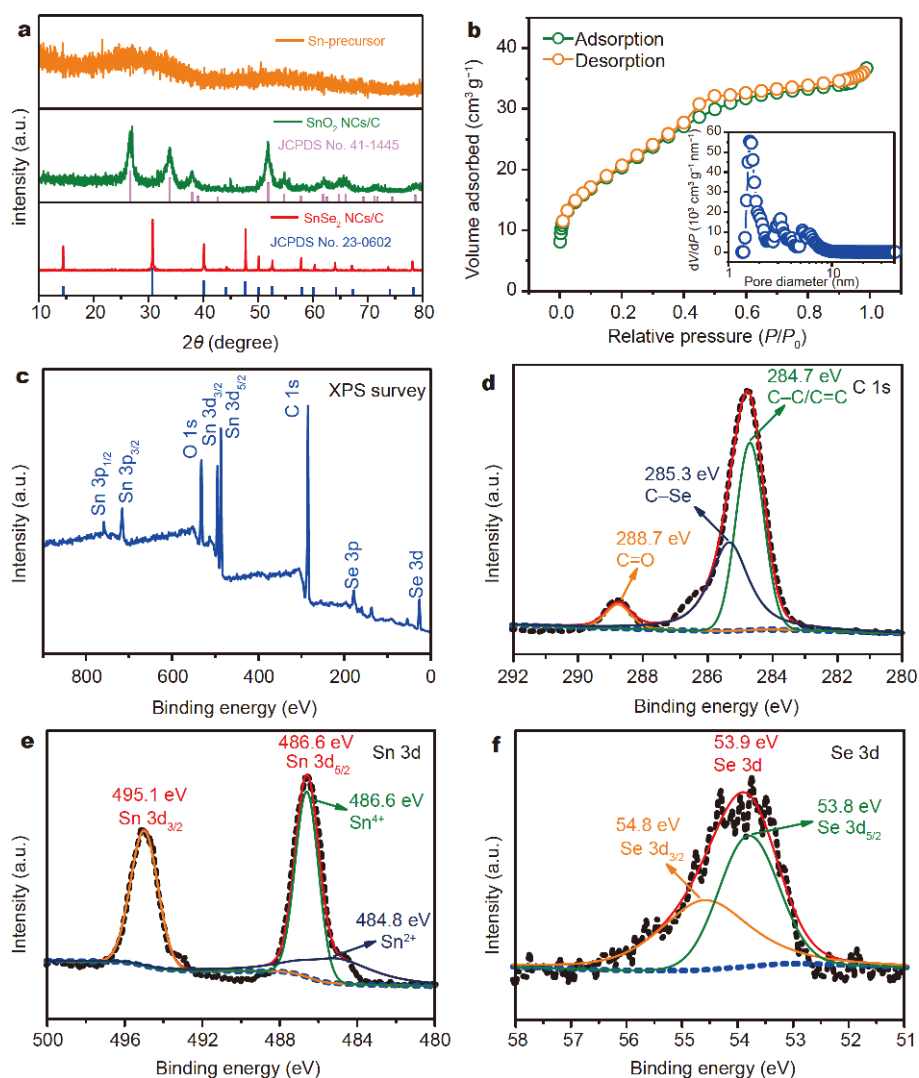


**Figure 3** (a) PXRD patterns of the as-synthesized Sn-precursor, SnO<sub>2</sub> NCs/C, and SnSe<sub>2</sub> NCs/C microspheres. (b) Nitrogen adsorption-desorption isotherms and pore size distribution (the inset) of SnSe<sub>2</sub> NCs/C microspheres. XPS spectra of the SnSe<sub>2</sub> NCs/C microspheres survey (c), C 1s (d), Sn 3d (e), and Se 3d (f).

tion and states of the elements on the surface of SnSe<sub>2</sub> NCs/C, X-ray photoelectron spectroscopy (XPS) was carried out (Fig. 3c–f). The survey spectrum demonstrates the presence of Sn, Se, and C in the SnSe<sub>2</sub> NCs/C (Fig. 3c). The high resolution C 1s spectrum in Fig. 3d shows three peaks at 284.7, 285.3, and 288.7 eV, corresponding to sp<sup>2</sup>-hybridize C, –C–Se, and C=O, respectively [29]. As shown in Fig. 3e, the peaks located at 486.6 and 495.1 eV can be assigned to Sn 3d<sub>5/2</sub> and Sn 3d<sub>3/2</sub>, respectively. In accordance with the fitting results, Sn<sup>2+</sup> valence state (484.8 eV) only occupies for a very small portion compared with the intense peak of Sn<sup>4+</sup> valence state at 486.6 eV, suggesting that Sn<sup>4+</sup> rather than Sn<sup>2+</sup> is the predominant form of Sn in the as-prepared sample [33]. In addition, the binding energies of 53.9 and 54.8 eV correspond well with Se 3d<sub>5/2</sub> and Se 3d<sub>3/2</sub> (Fig. 3f),

confirming the oxidation state of Se<sup>2-</sup> [34].

### Electrochemical characterization

The electrochemical performance of the SnSe<sub>2</sub> NCs/C sample was investigated in 2032 coin cells *via* assembling the electrode into sodium half-cell. Fig. 4a presents the initial five cyclic voltammogram (CV) curves of the SnSe<sub>2</sub> NCs/C composite in the voltage range of 0.01–3.0 V (*vs.* Na<sup>+</sup>/Na) at the scan rate of 0.1 mV s<sup>-1</sup>. In the initial cathodic sweep, three strong peaks at 1.67, 1.36 and 0.98 V, which disappear in the following four cycles, can be attributed to the initial insertion of sodium ion in SnSe<sub>2</sub> interlayers with the formation of Na<sub>x</sub>SnSe<sub>2</sub> (Equation (1)), similar to the lithium and sodium insertion of SnS<sub>2</sub> layer [35,36]. The sharp peak at 0.67 V in the first cycle decreases in the second cycle, which is caused by the

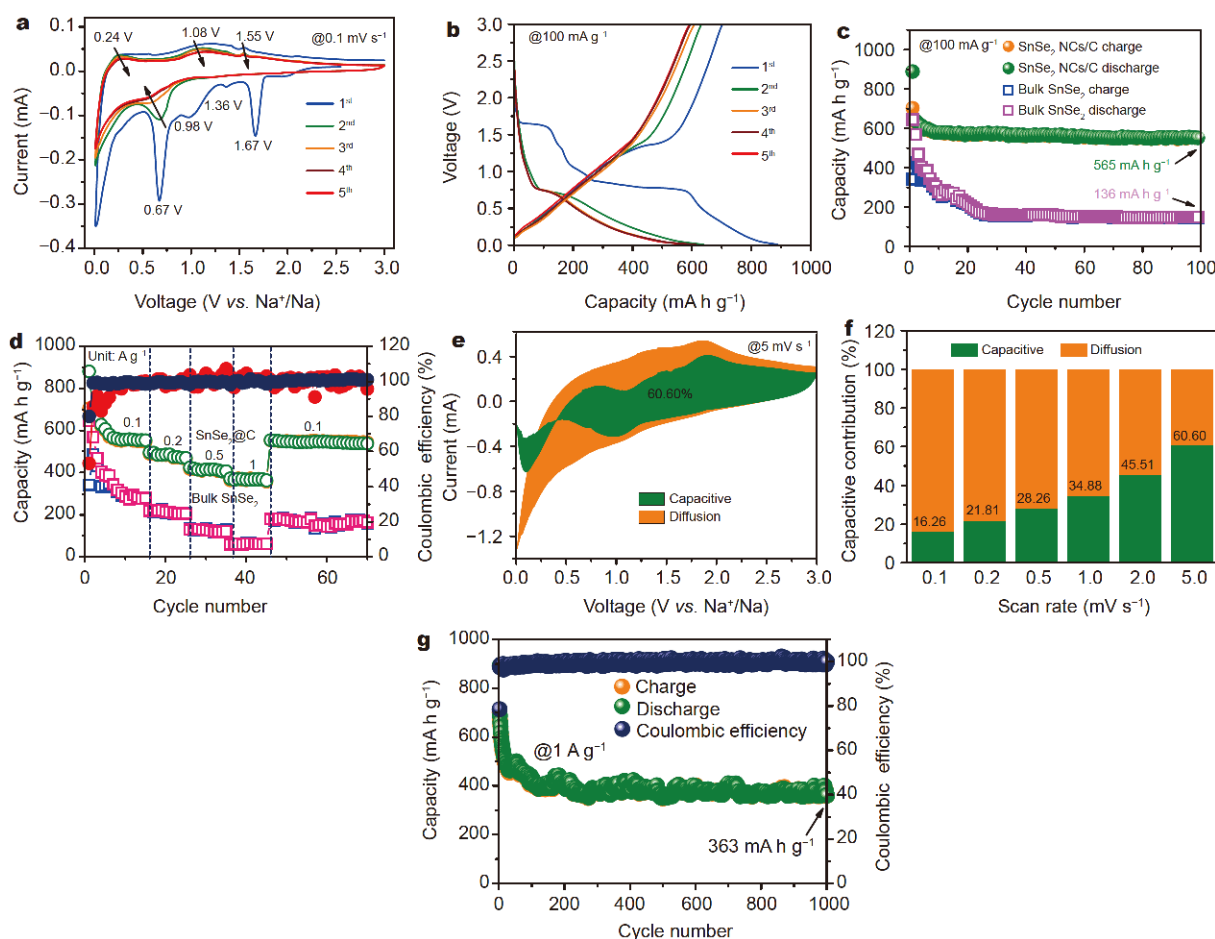


**Figure 4** (a) CV curves of the SnSe<sub>2</sub> NCs/C in the first five cycles at a scan rate of 0.1 mV s<sup>-1</sup>. (b) Charge-discharge profiles for the SnSe<sub>2</sub> NCs/C at 100 mA g<sup>-1</sup> in the first five cycles. (c) Cycling performances of the SnSe<sub>2</sub> NCs/C and bulk SnSe<sub>2</sub> at 100 mA g<sup>-1</sup> for 100 cycles. (d) Rate performances of the SnSe<sub>2</sub> NCs/C and bulk SnSe<sub>2</sub> at various current densities from 0.1 to 1 A g<sup>-1</sup>. (e) CV curve with the pseudocapacitive contribution shown in the olive region at a scan rate of 5 mV s<sup>-1</sup>. (f) The bar chart shows the contribution ratios of capacitive capacity and diffusion-limited capacity at various scan rates. (g) Long-term cycle performance of SnSe<sub>2</sub> NCs/C at 1 A g<sup>-1</sup> for 1000 cycles.

reduction of SnSe<sub>2</sub> to metallic Sn, the formation of Na<sub>2</sub>Se, and the formation of irreversible solid electrolyte interphase (SEI) layer (Equation (2)) [37,38]. During the initial anodic sweep, the broad peaks at near 0.24 and 1.08 V are attributed to the conversion process from metallic Sn to Na<sub>3.75</sub>Sn (Equation (3)), while the peak at 1.55 V is related to the restitution process with the formation of SnSe<sub>2</sub> [29,39]. Furthermore, the overlapping CV curves between the fourth and fifth cycles suggest the potentially excellent cycling capability of SnSe<sub>2</sub> NCs/C.

Based on the previous reports on the SnSe<sub>2</sub> anode for Na storage, the initial charging process can be attributed to the intercalation and conversion reactions [29]:



The subsequent charging/discharging cycles were characterized by reversibly alloying and de-alloying Sn and Na<sub>3.75</sub>Sn [29]:

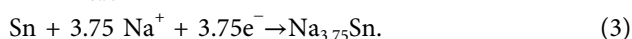


Fig. 4b shows the typical galvanostatic charge-discharge profiles of the SnSe<sub>2</sub> NCs/C electrode for the first five cycles in the voltage range of 0.01–3.0 V at a current density of 100 mA g<sup>-1</sup>. The charge-discharge voltage plateaus, corresponding to the different stage phase transformations, can be well distinguished, in good agreement with the CV results. For instance, the initial discharge voltage plateau located at 1.67 V, which disappears in the following cycles, is ascribed to the irreversible intercalation of sodium ions into SnSe<sub>2</sub> interlayers. In addition, the broad plateaus at 0.45–0.95 V (for the discharge process) and 0.85–1.55 V (for the charging process) represent the contribution from the reversible sodium ion insertion/extraction.

The first discharge and charge steps deliver specific capacity values of 885 and 702 mA h g<sup>-1</sup>, respectively, corresponding to a high initial coulombic efficiency (CE) of 79%, and the capacity loss is considered to be caused by the formation of irreversible SEI film on the surface of the electrode and the decomposition of electrolyte. Furthermore, the charge-discharge curves nearly overlap with each other except for the first two cycles, which indicates the high reversibility of the SnSe<sub>2</sub> NCs/C as an anode material for SIBs. One most impressive feature of the SnSe<sub>2</sub> NCs/C electrode is the cyclicity. As shown in Fig. 4c, the SnSe<sub>2</sub> NCs/C electrode achieves a stable capacity of 565 mA h g<sup>-1</sup> after 100 cycles at a current density of 100 mA g<sup>-1</sup>, accounting for 96.4% of the capacity of the 7<sup>th</sup> cycle, while the bulk SnSe<sub>2</sub> electrode only retains a capacity of 136 mA g<sup>-1</sup>. These results indicate that the

anode materials with high conductivity and low volume change are favored to enhance the cycle performance and reversible capacity of SIBs. Fig. S4 shows the electrochemical impedance spectroscopy (EIS) measurements of the bulk SnSe<sub>2</sub> and SnSe<sub>2</sub> NCs/C anode at open circuit voltage and after the 20<sup>th</sup> cycle. It is shown that the diameter of the semicircle for SnSe<sub>2</sub> NCs/C anode is much smaller than that of the bulk SnSe<sub>2</sub> anode in SIBs after the 20<sup>th</sup> cycle, suggesting lower charge-transfer resistance (*R*<sub>ct</sub>), which can be ascribed to the good conductivity and stable electrode/electrolyte interface.

High rate capacity is a key parameter to assess the electrochemical performance of electrode materials, and the SnSe<sub>2</sub> NCs/C electrode exhibits a robust rate capability. As shown in Fig. 4d, the SnSe<sub>2</sub> NCs/C demonstrates a capacity of 548 mA h g<sup>-1</sup> at a galvanostatic rate of 0.1 A g<sup>-1</sup>, and 472, 414, and 366 mA h g<sup>-1</sup> at rates of 0.2, 0.5, and 1 A g<sup>-1</sup>, respectively. Moreover, when the current density is restored to 0.1 A g<sup>-1</sup>, the reversible capacity can revert to 536 mA h g<sup>-1</sup>, indicating the good reversibility. However, the rate performance of the bulk SnSe<sub>2</sub> anode was inferior, only showing the capacities of 281, 206, 121, and 62 mA h g<sup>-1</sup> under rates of 0.1, 0.2, 0.5, and 1 A g<sup>-1</sup>, respectively. When the current density was set back to 0.1 A g<sup>-1</sup>, only a reversible capacity of 167 mA h g<sup>-1</sup> was preserved. Compared with the bulk SnSe<sub>2</sub> electrode, the SnSe<sub>2</sub> NC/C composite electrodes demonstrate a high reversible specific capacity and an excellent cyclic performance (Fig. 4c), which can be attributed to the following aspects: (1) the SnSe<sub>2</sub> NCs/C microspheres inhibit the agglomeration of SnSe<sub>2</sub> nanocrystals by separating them from each other, and also greatly improve the conductivity as well as availability of electrode materials. (2) The 3D hierarchical porous structure not only enhances the contact area between the electrode and electrolyte, but also helps to suppress the volume expansion during the charge-discharge processes. (3) The SnSe<sub>2</sub> nanocrystals are small and uniformly anchor on the carbon networks, and thus accelerate the diffusion kinetics of electrons/ions and improve its structural stability.

In order to investigate the reason why the SnSe<sub>2</sub> NCs/C electrode has such an excellent rate capability, the charge storage behavior and reaction kinetics were conducted by correlating the currents (*i*) with sweep rate (*v*) based on Equation (4) [40]:

$$i = av^b, \quad (4)$$

where *b* reflects the charge storage behavior, as shown in Fig. S5. Typically, *b* indicates the diffusion controlled process (battery behavior), and the *b* value of 1.0 means

the surface capacitance controlled process (capacitor behavior). Fig. S6 shows the linear relationships between  $\log(i)$  and  $\log(v)$ . The  $b$  values of the anodic peak of SnSe<sub>2</sub> NCs/C is 0.86, indicating that Na-ion storage is mainly controlled by surface capacitance in the discharge process. The  $b$  values of the three cathodic peaks of SnSe<sub>2</sub> NCs/C are calculated to be 0.65, 0.62, and 0.75, implying the diffusion and surface capacitance controlled behavior coexisted in the charge process. To further quantify the storage contribution for SnSe<sub>2</sub> NCs/C, the current ( $i$ ) was separated at a fixed voltage ( $V$ ) based on the following equation [41–53]:

$$i(V) = k_1 v + k_2 v^{1/2}, \quad (5)$$

where  $k_1 v$  stands for the capacitive contribution, whereas  $k_2 v^{1/2}$  represents the diffusion-controlled contribution, and the constants  $k_1$  and  $k_2$  are obtained from the linear plots of  $i(V)/v^{1/2}$  vs.  $v^{1/2}$  at a certain voltage. As shown in Fig. 4e, the capacitive capacity contribution to the total charge for SnSe<sub>2</sub> NCs/C electrode is 60.6% at a scan rate of 5 mV s<sup>-1</sup>. Moreover, the capacitive contribution in CV curve at other scan rates is shown in Fig. S7. Fig. 4f shows the corresponding bar chart of the contribution ratios of capacitive behavior at various scan rates, which reveals that the capacitive contribution dominates gradually with the increase of scan rate, suggesting the noticeable enhancement in the rate performance of the SnSe<sub>2</sub> NCs/C electrode. As shown in Fig. 4g, the SnSe<sub>2</sub> NCs/C electrode exhibits excellent long-term cycling performance, retaining a capacity of 363 mA h g<sup>-1</sup> over 1000 cycles at a high current density of 1 A g<sup>-1</sup>, which represents the best superior cycle stability in all the reported tin selenides based anode materials for SIBs (Table S1).

## CONCLUSION

In summary, SnSe<sub>2</sub> nanocrystals coupled with hierarchical porous carbon microspheres can be used as a remarkable anode material for SIBs. The unusual structural and compositional features of the as-obtained SnSe<sub>2</sub> NCs/C can inhibit the agglomeration of SnSe<sub>2</sub> nanoparticles, relieve the volume expansion, accelerate the diffusion kinetics of electrons/ions, enhance the contact area between the electrode and electrolyte, and improve the structural stability of the composite. The SIBs with SnSe<sub>2</sub> NCs/C microspheres as anode materials show superior electrochemical properties (565 mA h g<sup>-1</sup> after 100 cycles at 100 mA g<sup>-1</sup>), excellent rate capability, and ultralong cycling stability (363 mA h g<sup>-1</sup> at 1 A g<sup>-1</sup> after 1000 cycles). This study provides valuable guidance for rationally developing advanced electrode materials for high per-

formance SIBs.

Received 11 September 2019; accepted 4 December 2019;  
published online 30 December 2019

- Dunn B, Kamath H, Tarascon JM. Electrical energy storage for the grid: A battery of choices. *Science*, 2011, 334: 928–935
- Shen L, Yu Y. Greener and cheaper. *Nat Energy*, 2017, 2: 836–837
- Larcher D, Tarascon JM. Towards greener and more sustainable batteries for electrical energy storage. *Nat Chem*, 2015, 7: 19–29
- Luo W, Shen F, Bommier C, *et al.* Na-ion battery anodes: Materials and electrochemistry. *Acc Chem Res*, 2016, 49: 231–240
- Firouzi A, Qiao R, Motallebi S, *et al.* Monovalent manganese based anodes and co-solvent electrolyte for stable low-cost high-rate sodium-ion batteries. *Nat Commun*, 2018, 9: 861
- Xiang X, Zhang K, Chen J. Recent advances and prospects of cathode materials for sodium-ion batteries. *Adv Mater*, 2015, 27: 5343–5364
- Yu L, Wang LP, Liao H, *et al.* Understanding fundamentals and reaction mechanisms of electrode materials for Na-ion batteries. *Small*, 2018, 14: 1703338
- Li Z, Bommier C, Chong ZS, *et al.* Mechanism of Na-ion storage in hard carbon anodes revealed by heteroatom doping. *Adv Energy Mater*, 2017, 7: 1602894
- Park H, Kwon J, Choi H, *et al.* Microstructural control of new intercalation layered titanoniobates with large and reversible  $d$ -spacing for easy Na<sup>+</sup> ion uptake. *Sci Adv*, 2017, 3: e1700509
- Wu T, Jing M, Yang L, *et al.* Controllable chain-length for covalent sulfur-carbon materials enabling stable and high-capacity sodium storage. *Adv Energy Mater*, 2019, 9: 1803478
- Fang Y, Liu Q, Xiao L, *et al.* A fully sodiated NaVOPO<sub>4</sub> with layered structure for high-voltage and long-lifespan sodium-ion batteries. *Chem*, 2018, 4: 1167–1180
- Wang S, Xia L, Yu L, *et al.* Free-standing nitrogen-doped carbon nanofiber films: integrated electrodes for sodium-ion batteries with ultralong cycle life and superior rate capability. *Adv Energy Mater*, 2016, 6: 1502217
- Li Y, Mu L, Hu YS, *et al.* Pitch-derived amorphous carbon as high performance anode for sodium-ion batteries. *Energy Storage Mater*, 2016, 2: 139–145
- Pan H, Hu YS, Chen L. Room-temperature stationary sodium-ion batteries for large-scale electric energy storage. *Energy Environ Sci*, 2013, 6: 2338
- Nie Z, Fava D, Kumacheva E, *et al.* Self-assembly of metal-polymer analogues of amphiphilic triblock copolymers. *Nat Mater*, 2007, 6: 609–614
- Ma D, Li Y, Mi H, *et al.* Robust SnO<sub>2-x</sub> nanoparticle-impregnated carbon nanofibers with outstanding electrochemical performance for advanced sodium-ion batteries. *Angew Chem Int Ed*, 2018, 57: 8901–8905
- Miao C, Liu M, He YB, *et al.* Monodispersed SnO<sub>2</sub> nanospheres embedded in framework of graphene and porous carbon as anode for lithium ion batteries. *Energy Storage Mater*, 2016, 3: 98–105
- Zhao K, Zhang L, Xia R, *et al.* SnO<sub>2</sub> quantum dots@graphene oxide as a high-rate and long-life anode material for lithium-ion batteries. *Small*, 2016, 12: 588–594
- Liang J, Yu XY, Zhou H, *et al.* Bowl-like SnO<sub>2</sub>@carbon hollow particles as an advanced anode material for lithium-ion batteries. *Angew Chem Int Ed*, 2014, 53: 12803–12807
- Xiong X, Yang C, Wang G, *et al.* SnS nanoparticles electrostatically

- anchored on three-dimensional N-doped graphene as an active and durable anode for sodium-ion batteries. *Energy Environ Sci*, 2017, 10: 1757–1763
- 21 He P, Fang Y, Yu XY, *et al.* Hierarchical nanotubes constructed by carbon-coated ultrathin SnS nanosheets for fast capacitive sodium storage. *Angew Chem Int Ed*, 2017, 56: 12202–12205
- 22 Liu Y, Yu XY, Fang Y, *et al.* Confining SnS<sub>2</sub> ultrathin nanosheets in hollow carbon nanostructures for efficient capacitive sodium storage. *Joule*, 2018, 2: 725–735
- 23 Luo B, Fang Y, Wang B, *et al.* Two dimensional graphene–SnS<sub>2</sub> hybrids with superior rate capability for lithium ion storage. *Energy Environ Sci*, 2012, 5: 5226–5230
- 24 Jiang Y, Wei M, Feng J, *et al.* Enhancing the cycling stability of Na-ion batteries by bonding SnS<sub>2</sub> ultrafine nanocrystals on amino-functionalized graphene hybrid nanosheets. *Energy Environ Sci*, 2016, 9: 1430–1438
- 25 Xu Y, Peng B, Mulder FM. A high-rate and ultrastable sodium ion anode based on a novel Sn<sub>4</sub>P<sub>3</sub>-P@graphene nanocomposite. *Adv Energy Mater*, 2018, 8: 1701847
- 26 Li Q, Li Z, Zhang Z, *et al.* Low-temperature solution-based phosphorization reaction route to Sn<sub>4</sub>P<sub>3</sub>/reduced graphene oxide nanohybrids as anodes for sodium ion batteries. *Adv Energy Mater*, 2016, 6: 1600376
- 27 Wang W, Li P, Zheng H, *et al.* Ultrathin layered snse nanoplates for low voltage, high-rate, and long-life alkali-ion batteries. *Small*, 2017, 13: 1702228
- 28 Yuan S, Zhu YH, Li W, *et al.* Surfactant-free aqueous synthesis of pure single-crystalline SnSe nanosheet clusters as anode for high energy- and power-density sodium-ion batteries. *Adv Mater*, 2017, 29: 1602469
- 29 Zhang F, Xia C, Zhu J, *et al.* SnSe<sub>2</sub> 2D anodes for advanced sodium ion batteries. *Adv Energy Mater*, 2016, 6: 1601188
- 30 Choi J, Jin J, Jung IG, *et al.* SnSe<sub>2</sub> nanoplate–graphene composites as anode materials for lithium ion batteries. *Chem Commun*, 2011, 47: 5241–5243
- 31 Wei Z, Wang L, Zhuo M, *et al.* Layered tin sulfide and selenide anode materials for Li- and Na-ion batteries. *J Mater Chem A*, 2018, 6: 12185–12214
- 32 Xiang Huang Z, Liu B, Kong D, *et al.* SnSe<sub>2</sub> quantum dot/rGO composite as high performing lithium anode. *Energy Storage Mater*, 2018, 10: 92–101
- 33 Sun W, Rui X, Yang D, *et al.* Two-dimensional tin disulfide nanosheets for enhanced sodium storage. *ACS Nano*, 2015, 9: 11371–11381
- 34 Yao J, Liu B, Ozden S, *et al.* 3D nanostructured molybdenum diselenide/graphene foam as anodes for long-cycle life lithium-ion batteries. *Electrochim Acta*, 2015, 176: 103–111
- 35 Qu B, Ma C, Ji G, *et al.* Layered SnS<sub>2</sub>-reduced graphene oxide composite—a high-capacity, high-rate, and long-cycle life sodium-ion battery anode material. *Adv Mater*, 2014, 26: 3854–3859
- 36 Jiang X, Yang X, Zhu Y, *et al.* *In situ* assembly of graphene sheets-supported SnS<sub>2</sub> nanoplates into 3D macroporous aerogels for high-performance lithium ion batteries. *J Power Sources*, 2013, 237: 178–186
- 37 Ko YN, Choi SH, Park SB, *et al.* Hierarchical MoSe<sub>2</sub> yolk–shell microspheres with superior Na-ion storage properties. *Nanoscale*, 2014, 6: 10511–10515
- 38 Zhou X, Wan LJ, Guo YG. Binding SnO<sub>2</sub> nanocrystals in nitrogen-doped graphene sheets as anode materials for lithium-ion batteries. *Adv Mater*, 2013, 25: 2152–2157
- 39 Zhai C, Du N, Zhang H, *et al.* Multiwalled carbon nanotubes anchored with SnS<sub>2</sub> nanosheets as high-performance anode materials of lithium-ion batteries. *ACS Appl Mater Interfaces*, 2011, 3: 4067–4074
- 40 Yang C, Feng J, Lv F, *et al.* Metallic graphene-like VSe<sub>2</sub> ultrathin nanosheets: superior potassium-ion storage and their working mechanism. *Adv Mater*, 2018, 30: 1800036
- 41 Wang W, Jiang B, Qian C, *et al.* Pistachio-shuck-like MoSe<sub>2</sub>/C core/shell nanostructures for high-performance potassium-ion storage. *Adv Mater*, 2018, 30: 1801812
- 42 Xiao Y, Su D, Wang X, *et al.* CuS microspheres with tunable interlayer space and micropore as a high-rate and long-life anode for sodium-ion batteries. *Adv Energy Mater*, 2018, 8: 1800930
- 43 Fang G, Wang Q, Zhou J, *et al.* Metal organic framework-templated synthesis of bimetallic selenides with rich phase boundaries for sodium-ion storage and oxygen evolution reaction. *ACS Nano*, 2019, 13: 5635–5645
- 44 Cai Y, Cao X, Luo Z, *et al.* Caging Na<sub>3</sub>V<sub>2</sub>(PO<sub>4</sub>)<sub>2</sub>F<sub>3</sub> microcubes in cross-linked graphene enabling ultrafast sodium storage and long-term cycling. *Adv Sci*, 2018, 5: 1800680
- 45 Feng Y, Chen S, Wang J, *et al.* Carbon foam with microporous structure for high performance symmetric potassium dual-ion capacitor. *J Energy Chem*, 2020, 43: 129–138
- 46 Liu X, Zhao L, Wang S, *et al.* Hierarchical-structure anatase TiO<sub>2</sub> with conductive network for high-rate and high-loading lithium-ion battery. *Sci Bull*, 2019, 64: 1148–1151
- 47 Liu R, Liang Z, Gong Z, *et al.* Research progress in multielectron reactions in polyanionic materials for sodium-ion batteries. *Small Methods*, 2018, 3: 1800221
- 48 Wang WA, Huang H, Wang B, *et al.* A new dual-ion battery based on amorphous carbon. *Sci Bull*, 2019, 64: 1634–1642
- 49 Hao J, Peng S, Qin T, *et al.* Fabrication of hybrid Co<sub>3</sub>O<sub>4</sub>/NiCo<sub>2</sub>O<sub>4</sub> nanosheets sandwiched by nanoneedles for high-performance supercapacitors using a novel electrochemical ion exchange. *Sci China Mater*, 2017, 60: 1168–1178
- 50 Guo S, Sun Y, Liu P, *et al.* Cation-mixing stabilized layered oxide cathodes for sodium-ion batteries. *Sci Bull*, 2018, 63: 376–384
- 51 Xu ZL, Park J, Yoon G, *et al.* Graphitic carbon materials for advanced sodium-ion batteries. *Small Methods*, 2018, 3: 1800227
- 52 Jiang H, Zhao T, Ren Y, *et al.* *Ab initio* prediction and characterization of phosphorene-like SiS and SiSe as anode materials for sodium-ion batteries. *Sci Bull*, 2017, 62: 572–578
- 53 Li M, Yang W, Huang Y, *et al.* Hierarchical mesoporous Co<sub>3</sub>O<sub>4</sub>@ZnCo<sub>2</sub>O<sub>4</sub> hybrid nanowire arrays supported on Ni foam for high-performance asymmetric supercapacitors. *Sci China Mater*, 2018, 61: 1167–1176

**Acknowledgements** This work was supported by the National Key R&D Research Program of China (2016YFB0100201), Beijing Natural Science Foundation (JQ18005), the National Natural Science Foundation of China (51671003, 21802003), China Postdoctoral Science Foundation (2019TQ0001), and the start-up supports from Peking University and Young Thousand Talented Program.

**Author contributions** Guo S conceived the project and directed the experiment. Chen H designed the experiments. Chen H, Mu Z and Li Y prepared and carried out the main experiments and characterization. Chen H wrote the manuscript. All authors contributed to the data analysis, discussed the results, and commented on the manuscript.

**Conflict of interest** The authors declare no conflict of interest.

**Supplementary information** Experimental details and supporting data are available in the online version of the paper.



**Hui Chen** is a PhD student of the University of Electronic Science and Technology of China under the supervision of Prof. Jinshu Wang. Currently, he is studying at Peking University as an exchange student in Prof. Shaojun Guo's group. His research interests include the synthesis and characterization of nanomaterials for alkali-ion batteries, photocatalysis and perovskite solar cells.



**Shaojun Guo** received his BSc degree in Jilin University (2005) and PhD degree in the Chinese Academy of Sciences (2010). He worked as a postdoctoral researcher associate at Brown University (2011–2013) and as a prestigious Oppenheimer Distinguished Fellow at Los Alamos National Laboratory (2013–2015). He joined the College of Engineering, Peking University in 2015 and is currently a Professor. His research interests focus on engineering nanocrystals and 2D materials for catalysis, renewable energy,

optoelectronics and biosensors.

## SnSe<sub>2</sub>纳米晶耦合分层多孔碳微球作为长寿命钠离子电池负极材料

陈辉<sup>1,2,3</sup>, 慕梓杰<sup>1</sup>, 李一举<sup>1</sup>, 夏仲宏<sup>1</sup>, 杨勇<sup>1</sup>, 吕帆<sup>1</sup>, 周金辉<sup>1</sup>, 晁玉广<sup>1</sup>, 王金淑<sup>2</sup>, 王宁<sup>2,3</sup>, 郭少军<sup>1,4,5\*</sup>

**摘要** 硒化锡用于钠离子电池负极时具有较高的理论比容量且其成本低廉, 因而备受关注. 然而, 由于其固有的低导电性, 以及在充放电过程中的缓慢动力学和体积膨胀, 硒化锡作为钠离子电池负极材料表现出的性能较差. 本文首次合成SnSe<sub>2</sub>纳米晶耦合分层多孔碳微球(SnSe<sub>2</sub> NCs/C)用于增强钠离子电池的比容量、倍率能力和持久性. SnSe<sub>2</sub> NCs/C独特的结构可以有效阻止SnSe<sub>2</sub>纳米晶的团聚, 减轻材料体积膨胀, 加快电子和离子的扩散, 增大电解液与电极材料的接触面积, 提高材料结构的稳定性. 所制备的SnSe<sub>2</sub> NCs/C微球具有较高的可逆比容量(在100 mA g<sup>-1</sup>的电流密度下循环100圈后仍保持565 mA h g<sup>-1</sup>的比容量), 出色的倍率能力和长循环寿命稳定性(在1 A g<sup>-1</sup>的电流密度下循环1000圈后仍保持363 mA h g<sup>-1</sup>的比容量).